Earth and Planetary Science Letters 449 (2016) 79–88

Contents lists available at ScienceDirect

Earth and Planetary Science Letters

www.elsevier.com/locate/epsl

A new perspective on West African hydroclimate during the last deglaciation

Andrew O. Parker [a,*], Matthew W. Schmidt [b], Zane R. Jobe [c], Niall C. Slowey [a]

[a] Department of Oceanography, Texas A&M University, College Station, TX 77843, United States
[b] Department of Ocean, Earth and Atmospheric Sciences, Old Dominion University, Norfolk, VA 23529, United States
[c] Shell Projects and Technology, Houston, TX 77082, United States

ARTICLE INFO

Article history:
Received 20 November 2015
Received in revised form 22 May 2016
Accepted 23 May 2016
Available online 7 June 2016
Editor: M. Frank

Keywords:
West African Monsoon
African humid period
deglacial climate
foraminiferal geochemistry
X-ray fluorescence

ABSTRACT

Widespread drought characterized the Heinrich 1 and Younger Dryas cold periods of the last deglaciation throughout much of Africa, causing large increases in dust emissions from the Sahara and Sahel. At the same time, increases in wind strength may have also contributed to dust flux, making it difficult to interpret dust records alone as reflecting changes in rainfall over the region. The Niger River has the third largest drainage basin in Africa and drains most of the Sahara and Sahel and thus preserves and propagates climatic signals. Here, we present new reconstructions of Niger Delta sea surface salinity and Niger River discharge for the last 20,000 years in order to more accurately reconstruct the onset of the Western African Monsoon system. Based on calculated $\delta^{18}O_{SEAWATER}$ ($\delta^{18}O_{SW}$) and measured Ba/Ca ratios in planktonic foraminifera, these new records reflect changes in sub-Saharan precipitation across the Niger River Basin in West Africa and reveal that the West African Monsoon system began to intensify several thousand years after the equatorial Monsoon system in Central Africa. We also present new records of primary productivity in the Niger Delta that are related to wind-driven upwelling and show that productivity is decoupled from changes in Niger River discharge. Our results suggest that wind strength, rather than changes in monsoon moisture, was the primary driver of dust emissions from the Sahara and Sahel across the last deglaciation.

1. Introduction

Prolonged droughts across West Africa impart significant socio-economic hardships on developing nations. Complex interactions between the ocean, land, atmosphere, and local solar insolation result in non-linear feedbacks that make understanding past and future climate changes in this part of the world extremely difficult (deMenocal et al., 2000). These complexities are exemplified in paleo-hydrological reconstructions from West Africa, where the deglacial history of precipitation varies as a function of both proxy and location. Northwest African proxy reconstructions of continental aridity, including dust flux and grain size records from continental slope sediment cores, point to a severe and widespread drought that characterized Heinrich Event 1 (H1, 16.7–15.1 kyr) (Collins et al., 2013; Mulitza et al., 2008; Stager et al., 2011; Tjallingii et al., 2008). During this time, dust emissions from the Sahara and Sahel were on average five times higher compared to the early Holocene humid interval (McGee et al., 2013). In contrast, previously published records of sea surface salinity (SSS) and river discharge from the eastern Gulf of Guinea, which have been interpreted to reflect West African precipitation runoff, suggest little or no change in West African runoff during H1 (Weldeab et al., 2007). A second discrepancy between regional precipitation proxies occurs during the deglacial cold reversal known as the Younger Dryas (YD, ~11.2–12.9 kyr). During this period, records from northwest Africa record much smaller increases in dust flux relative to H1, implying less intense drought conditions (Mulitza et al., 2008; Tjallingii et al., 2008), whereas SSS and river discharge records from the Gulf of Guinea suggest a severe reduction in riverine discharge during the YD (Weldeab et al., 2007). Clearly, questions surrounding the drought history of West Africa remain.

Another uncertainty in the interpretation of published dust records regards the extent to which wind speed versus aridity influences dust fluxes. During the H1 and YD cold reversals, steepened meridional temperature gradients in the North Atlantic resulted in stronger trade winds over West Africa (McGee et al., 2010). Intensified winds have the ability to increase dust mobilization, resulting in drought-like dust signals independent of hydroclimate change across the Sahara and Sahel during H1 and

* Correspondence to: 3146 TAMU, College Station, TX 77843, United States. Tel.: +1 720 227 4917.
E-mail address: parkerao@geos.tamu.edu (A.O. Parker).

http://dx.doi.org/10.1016/j.epsl.2016.05.038
0012-821X/

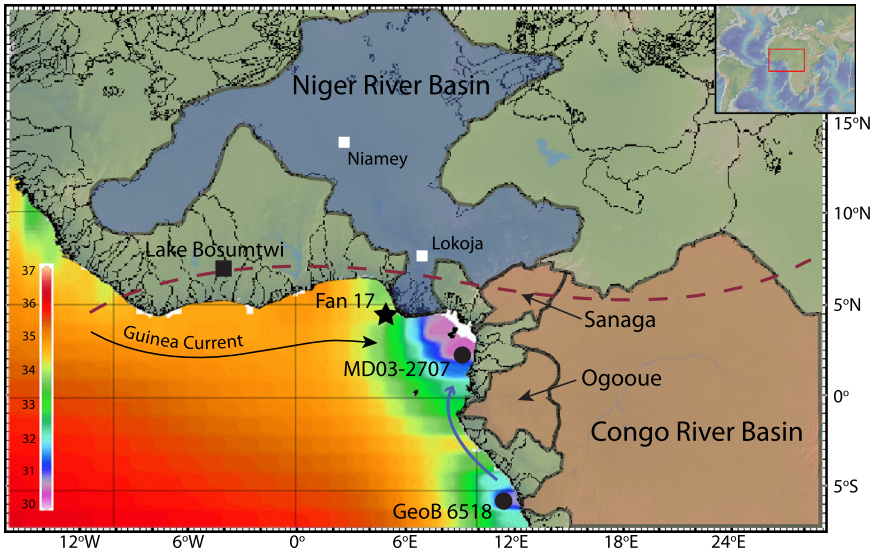

Fig. 1. Regional map of major West and Equatorial African river basins that drain into the Gulf of Guinea. Niger Delta core Fan 17 (black star) was recovered in 1178 m of water and less than 100 km equidistant from the two major Niger River distributaries. MD03-2707 (black circle) is located 400 km southeast of the Niger River Delta in the low salinity core for the Gulf of Guinea, where freshwater from the Niger and other major Central Africa rivers including the Congo River (blue arrow) also contribute to the low SSS. Red dashed line represents the approximate position of surface wind convergence during boreal winter. The Niger and Congo River drainage basins are outlined by shaded blue and brown, respectively. GeoB-6518 (black circle) is located near the mouth of the Congo River. (For interpretation of the references to color in this figure legend, the reader is referred to the web version of this article.)

the YD. Recently, observations linked wind strength, not aridity, as the most significant source of inter-annual to decadal variability of Saharan aerosol emissions (Ridley et al., 2014; Rodriguez et al., 2015), and modeling studies support the role of wind as a driver of enhanced deglacial dust flux (Murphy et al., 2014). Nevertheless, there is limited evidence of sub-Saharan hydroclimate change during the deglaciation to confirm aridity patterns, making it difficult to determine whether changes in continental aridity or wind strength played a more important role in driving deglacial dust emissions from the Sahara and Sahel.

In order to more accurately reconstruct temporal changes in the West African Monsoon (WAM) system across the last deglaciation, we present new records of hydrologic change in the Niger River drainage basin from sediment core Fan 17 (4.81°N, 4.45°E, 1178 m water depth) over the last 21 kyr based on stable oxygen isotopes and trace metal analyses on the planktonic foraminifera *Globigerinoides ruber*. We combine Mg/Ca-sea surface temperature (SST) estimates with measured $\delta^{18}O_{calcite}$ ($\delta^{18}O_c$) values to calculate $\delta^{18}O_{sw}$ values, a proxy for SSS. In addition, we measure Ba/Ca ratios in *G. ruber* as a proxy for past discharge variability from the Niger River. We then compare our results with $\delta^{18}O_{sw}$ and Ba/Ca records from a core located in the Gulf of Guinea, MD03-2707 (Weldeab et al., 2007), to explore subtle differences in the timing of regional monsoon development during the deglaciation. Core MD03-2707 is located farther east of Fan 17 in the low salinity core of the Gulf of Guinea, very close to equatorial river runoff. Using the differences between the Fan 17 and MD03-2707 Ba/Ca records, we show that monsoon onset over West Africa and the Sahel was more gradual than previously thought, and has important implications for the interpretation of deglacial dust records from the northwest coast of Africa.

2. Oceanographic setting

Sediment core Fan 17 was collected by Shell Oil in 2007 and donated to Texas A&M University for research purposes (Fig. 1). An intraslope sandy turbidite lobe deposit exists to the northwest of Fan 17, but seismic data indicates that Fan 17 is not disturbed by mass wasting or turbidity currents depositing sand on the intraslope lobe. Mean annual SST at the core location is 27.8 °C with less than 1 °C of seasonal variability. SSS in the Niger Delta ranges from 32 during the wet summer months to 34.5 during the dry winters, with an annual average of 33.4. The low SSS during the summer months is a direct result of the monsoon that develops across West Africa (Fig. 1). The Guinea Current running along the Guinea Coast moves discharge from the Niger River eastward. The location of Fan 17 close to the shelf break and roughly 100 km equidistant from the two main distributaries of the Niger River make it ideal for continuously monitoring river runoff regardless of changes in sea level or delta lobe avulsion. The current shelf break depth for the Niger Delta is ~90 m. Given global sea level was 120 m lower during the LGM, the shelf would have been exposed until after meltwater pulse-1A (MWP-1A) when sea-level abruptly rose 20 m to ~90 m below present. Thus, the freshwater plume would have been located even closer to the Fan 17 core site prior to the YD.

During boreal summer, differential heating between the land and ocean creates an onshore wind that transports moisture rich air from the Gulf of Guinea to a zone of ascent caused by the juxtaposition between the axes of two mid-level atmospheric jets (Nicholson, 2008). The resultant tropical rainbelt sets up over the Niger River Basin and is responsible for producing most of the rains associated with the seasonal monsoon throughout much of sub-Saharan West Africa, including the Sahel. Hydrographic data along the Niger River show that precipitation falling in the Sahelian latitudes of the Niger River Basin (12–18°N) is the main determinant of the magnitude of discharge at the Niger Delta, and riverine flow is therefore strongly related to the intensity of the rainbelt (Itiveh and Bigg, 2008). This discharge contributes to the very low salinities of the modern Gulf of Guinea (Fig. 1). However, the Niger River is not the only river that contributes to the low salinities in the Gulf of Guinea. Freshwater from the Ogooue and Congo rivers also contribute large amounts of runoff to the Gulf of Guinea along with other smaller equatorial rivers (Fig. 1).

3. Methods

3.1. Age model development

The age model for Fan 17 is based on 11 radiocarbon-dated intervals measured using accelerator mass spectrometry at Lawrence

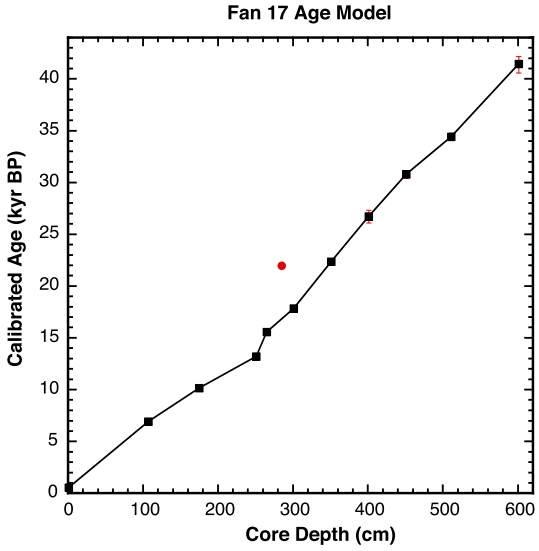

Fig. 2. Age model for Fan 17 is constrained by linear interpolation between 11 radiocarbon analyses converted to calendar years using CALIB 7.1. One out of sequence point was omitted at 285 cm (red circle). All radiocarbon analyses were performed at Lawrence Livermore National Laboratory.

Livermore National Laboratory (6 of which constrain the deglacial interval of our record). The ^{14}C ages were converted to calendar ages using the CALIB 7.1 program and a standard marine reservoir age correction of 400 years (Stuiver et al., 2013). One out-of-sequence date at 285 cm was not included in this age model (Fig. 2). The core is well preserved with no sedimentological evidence for turbidite layers disturbing the deglacial sequence. However, visual inspection of the core logs indicates evidence of enhanced bioturbation at around 285 cm in the core. This enhanced bioturbation could have mixed older sediments in this interval. Therefore, we omitted this sample from our age model. Assuming linear sedimentation rates between calibrated ages, the resulting age model yields a mean deglacial and Holocene sedimentation rate of ~16.9 cm/kyr (Fig. 2). Fan 17 was subsequently sampled at 2 cm intervals, corresponding to a temporal resolution of ~120 years.

3.2. Isotope measurements

Sediment samples from Fan 17 were disaggregated in ultra-pure deionized water and sieved with a 63 μm mesh. In order to limit ontogenetic and growth rate effects on shell geochemistry, *G. ruber* (pink) specimens were picked from the 250–355 μm size fraction. The pink variety of *G. ruber* was selected because its abundance was much higher than white *G. rubers* in the Fan 17 sediment samples and also was used in other reconstructions from this region (Weldeab et al., 2007). *G. ruber* tests were then sonicated for 5–10 s in methanol and analyzed whole on a Thermo Scientific MAT 253 IR-MS with Automated Kiel IV Carbonate Device at the Texas A&M College of Geoscience Stable Isotope Facility. 15–20 *G. ruber* tests per samples were analyzed in order to get a statistical average of the natural range in $\delta^{18}O$ variability within each population of foraminifera. Raw $\delta^{18}O$ values were standardized using NBS-19.

3.3. Trace metal measurements

We performed trace metal analyses on the same population and size fraction of *G. ruber* used for stable isotope analyses. Up to ~580 μg (~35–40 shells) of *G. ruber* (pink) were gently crushed between two glass slides, homogenized, and then split into duplicate samples for analysis. We followed established cleaning procedures of Schmidt et al. (2012a), which includes sonication in methanol to remove clays, a hot water bath in reducing agents to remove metal oxides, and a final hot water bath in oxidizing agents to remove organic material. Samples were then transferred into acid cleaned vials and leached with weak nitric acid. All clean work was conducted in laminar flow benches under trace metal clean conditions. Lastly, samples were analyzed in replicate on a Thermo Scientific Element XR High Resolution Inductively Coupled Plasma Mass Spectrometer at Texas A&M using isotope dilution. A suite of elements was analyzed including Na, Mg, Ba, U, Ca, Mn, Al and Fe. We excluded analyses with anomalously high Al/Ca (>100 μmol/mol), Mn/Ca and Fe/Ca (>200 μmom/mol), which indicated samples where detrital clays and digenetic coatings were not sufficiently removed during cleaning. We also rejected measurements with very low percent recovery (<10%) where the loss of shell material during trace metal cleaning was likely the result of human error.

3.4. XRF measurements

XRF data were obtained by scanning core Fan 17 at 1 cm intervals using an Avaatech X-ray Fluorescence core scanner at the International Ocean Discovery Program Gulf Coast Repository, at Texas A&M University. Reduction of these data followed the normalized median scaled (NMS) reduction procedures presented by Lyle et al. (2012). Briefly, we scaled the data to average upper crustal compositions using values from Taylor and Mclennan (1995), which converts the elemental peak areas into typical ranges of sediment composition. This scaling removes large disparities between X-ray fluorescence yield for different elements, e.g. for Al vs. Ca. To account for changes in sediment density arising from cracks and sediment porosity, we took the scaled XRF data and normalized the components to sum to 100%. The $CaCO_3$ component of the sediment was estimated by calibrating the XRF Ca NMS data with 20 discrete $CaCO_3$ measurements. CO_2 released from the sediment by acidification, assumed to be from $CaCO_3$, was measured using an Automate Prep Device to react weighted aliquots of bulk sediment with acid and a Coulometrics CO_2 Coulometer to measure the resultant % $CaCO_3$ of the sediment. Calibrating the XRF Ca to $CaCO_3$ is justified because aluminosilicate percentage of Ca is low and varies only slightly while carbonate Ca ranges from 1.6 to 12%, assuming the 4–30% estimate of carbonate content.

3.5. Calculations

We converted our Mg/Ca ratios to SST using the multi-species relationship of Anand et al. (2003):

$$\mathrm{Mg/Ca} = 0.38\exp(0.09 \times \mathrm{SST})(\mathrm{error} = \pm 0.5\,^{\circ}\mathrm{C}). \quad (1)$$

Given the shallow water depth of Fan 17 and the lack of visual evidence for significant dissolution of foraminiferal calcite, this equation best suits our record because it does not include a dissolution-corrected term needed for deeper locations. Furthermore, Hertzberg and Schmidt (2013) showed there was only a minor salinity effect on *G. ruber* Mg/Ca ratios, and argued that calibration equation (1) worked well for calculating SSTs in the Atlantic when using well preserved shell material. Then, we combine the Mg/Ca derived SST with measured $\delta^{18}O_c$ values to compute $\delta^{18}O_{sw}$ using the low-light relationship from Bemis et al. (1998):

$$\mathrm{SST}(^{\circ}\mathrm{C}) = 16.5 - 4.80\left(\delta^{18}O_c - \left(\delta^{18}O_{sw} - 0.27‰\right)\right). \quad (2)$$

Finally, during periods of enhanced continental ice storage, the oceans become enriched in ^{18}O relative to ^{16}O. We removed this effect of ice volume on our $\delta^{18}O_{sw}$ record using the sea-level record of Waelbroeck et al. (2002) where a maximum enrichment

of $\delta^{18}O$ at the LGM was equal to 1.04‰ enrichment of the ocean. The resulting record of ice-volume free (IVF) $\delta^{18}O_{sw}$ provides a measure of regional surface water $\delta^{18}O$ variability.

3.6. Error analysis

The long-term analytical precision for $\delta^{18}O$ measurements is less than ±0.07‰, based on the NBS-19 standard. Based on a synthetic, matrix-matched standard analyzed throughout this study, the analytical reproducibility for Mg/Ca is 1.13%. The pooled standard deviation of all replicate *G. ruber* Mg/Ca analyses is ±3.08% (1 SD, df = 103) based on 110 measured intervals. Given the average *G. ruber* Mg/Ca ratio for this study of 3.46 mmol/mol, this error equates to ±0.11 mmol/mol or ±0.71 °C. Similarly for Ba/Ca, the long-term analytical precision based on a matrix-matched standard is 2.02%. The pooled standard deviation is ±7.2% (1 SD, df = 103) based on 110 intervals. The average Ba/Ca ratio for this study is 1.14 µmol/mol which equates to an error of ±0.08 µmol/mol.

We calculated the 1σ error of the calculated $\delta^{18}O_{sw}$ values by propagating the 1σ analytical error from the Mg/Ca and $\delta^{18}O_c$ analyses, as well as the errors reported for the Mg/Ca:SST and $\delta^{18}O_c$:SST calibrations. The estimated 1σ error for the $\delta^{18}O_{sw}$ is ±0.24‰, which is consistent with reported error propagations from prior studies ranging between ±0.18‰ to ±0.26‰ (Schmidt and Lynch-Stieglitz, 2011; Schmidt et al., 2012a). To calculate the error on the smoothed IVF-$\delta^{18}O_{sw}$ we used the following equation: $\sigma = \sigma_{propogated}/\sqrt{n}$ (where n is the number of points used in the smoothing function). We acknowledge that additional error is introduced when the ice-volume correction is applied, but this error has not been included the final estimated error.

4. Results and discussion

4.1. Mg/Ca-SST record

The calculated Mg/Ca core-top SST for *G. ruber* in Fan 17 was 25.6 °C using equation (1). Modern mean annual SST at the Niger Delta is 27.8 °C with little seasonal variability. However, *G. ruber* does not live at the immediate water surface (0 m depth), but instead lives slightly deeper at depths between 10–40 m in the EEA (Steph et al., 2009). The mixed layer temperature at 30 m depth in the Niger Delta is 26.1 °C, making the calculated core top temperature within the calibration uncertainty and consistent with the depth habitat for *G. ruber*.

The Fan 17 *G. ruber* Mg/Ca derived SST record from the Niger Delta indicates a glacial–interglacial rise in EEA SST of 4 °C across the last deglaciation (Fig. 3B). Minimum temperatures of 22.1 °C characterized the LGM, with SST variability of ~1 °C between 17.5–20 kyr. By the start of H1, temperatures start to gradually increase from 22.1 °C at 17.5 kyr to 23.6 °C by 15 kyr (Fig. 3B). The Fan 17 record suggests SST increases by another degree at the start of the Bølling Allerød (BA) to 24.6 °C. At the start of the YD around 12.9 kyr, temperatures abruptly decrease by 1.5 °C and then rebound by 2 °C during the middle and later half of the YD from 12 to 11 kyr. A near modern temperature of 25.7 °C is reached during the early Holocene (Fig. 3). Temperatures during the Holocene vary between 24.4 and 26 °C for the duration of the Holocene.

H1 and the YD are thought to be associated with slowdowns of the Atlantic Meridional Overturning Circulation (AMOC) (McManus et al., 2004). Modeling studies have shown that the transmission of North Atlantic cooling to the tropical Atlantic during times of weak AMOC is transferred via both atmospheric and oceanic processes (Chang et al., 2008). In locations influenced by local upwelling, reorganizations of ocean circulation may also result in a warming of subsurface waters that is more significant than the cooling via the atmosphere during AMOC slowdown (Wan et al., 2009), thus

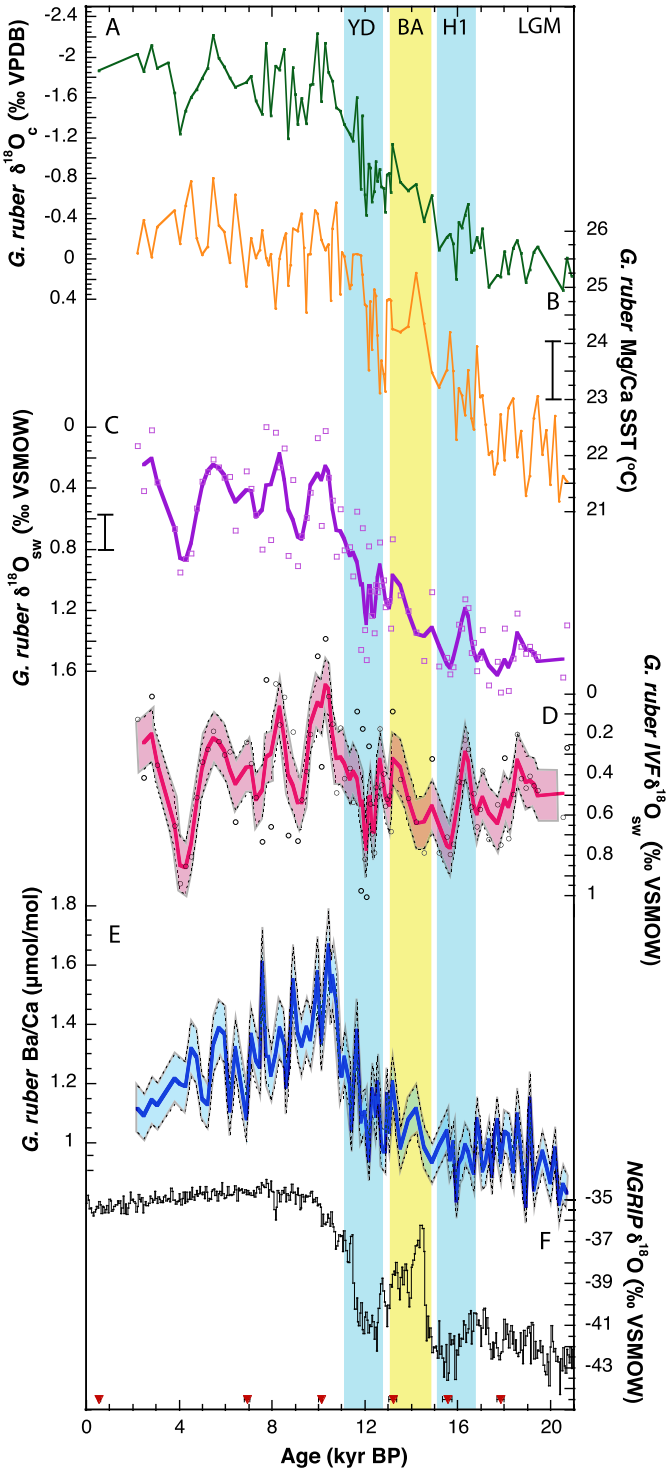

Fig. 3. Fan 17 *G. ruber* (A) $\delta^{18}O_c$, (B) Mg/Ca SST (°C) and calculated ±1σ error next to axis, (C) $\delta^{18}O_{sw}$ plotted as open purple squares with three-point weighted mean as purple line, and calculated ±1σ error for the smoothed record next to axis (D) IVF-$\delta^{18}O_{sw}$ plotted as grey circles with three point weighted mean as pink line. Pink shading represents the ±1σ error of the smoothed data (see text for details on how the error was calculated). (E) Ba/Ca ratios (µmol/mol) plotted as blue line with blue shading denoting the ±1σ error of the data and (F) NGRIP $\delta^{18}O$ for the last 21 kyr. Red triangles on the *x*-axis show the calibrated radiocarbon ages used in the age model and associated 2 sigma error bars. (For interpretation of the references to color in this figure legend, the reader is referred to the web version of this article.)

explaining why some locations across the tropical Atlantic record cooling during the YD, and others a warming. Modeling results suggest a warming of subsurface waters in the EEA during periods of reduced AMOC (Chang et al., 2008; Schmidt et al., 2012b). Therefore, the influence of coastal upwelling around the Niger Delta likely resulted in a warming during H1 as subsurface temperatures increased in response to an AMOC shutdown. In contrast, the cooling of surface waters at the start of the YD suggests that the effect of atmospheric cooling may have been greater during this time. Finally, both the *G. ruber* $\delta^{18}O_c$ and Mg/Ca-SST records indicate a warming during the second half of the YD (Fig. 3). This warming may be related to the reduced northward heat transport out of the tropical Atlantic when AMOC was reduced, as observed in other tropical Atlantic locations including the eastern tropical Atlantic, the Caribbean, and the Florida Straits (Schmidt and Spero, 2011; Schmidt and Lynch-Stieglitz, 2011).

In addition, the deglacial portion of our Fan 17 Mg/Ca SST record resembles a nearby record of *G. ruber* (pink) Mg/Ca-SST from core MD03-2707 in the Gulf of Guinea (Fig. 4A) (Weldeab et al., 2007). Consistent with a location east of Fan 17, the MD03-2707 Mg/Ca-SST record is roughly 1 °C warmer for the entire 0 to 20 kyr record, but shares the same magnitude of warming between the LGM and Holocene of ~4 °C. The MD03-2707 record also shows warming during H1 and indicates a slight warming across the YD. Similar trends in the deglacial temperature records in Fan 17 and the well-dated record of MD03-2707 also lend support to our age model.

4.2. IVF-$\delta^{18}O_{sw}$ record

Because $\delta^{18}O_{sw}$ varies linearly with SSS (Charles and Fairbanks, 1990), our IVF-$\delta^{18}O_{sw}$ can be used to estimate past changes in SSS. The Fan 17 IVF-$\delta^{18}O_{sw}$ record (Fig. 3D) shows that values during the LGM were close to the modern annual mean value of ~0.5‰. Nevertheless, our IVF-$\delta^{18}O_{sw}$ record suggests considerable variability during the period from the LGM until the start of the BA at 14.5 kyr, with a significant increase in IVF-$\delta^{18}O_{sw}$ values during H1. IVF-$\delta^{18}O_{sw}$ then steadily decreases from 0.8‰ to 0.4‰ during the BA (Fig. 3D). After a brief increase toward more positive values during the early YD, IVF-$\delta^{18}O_{sw}$ values abruptly decrease to the lightest values of 0.0‰ at 10 kyr. The Holocene record is characterized by several large oscillations of IVF-$\delta^{18}O_{sw}$ of about 1‰ (Fig. 3D).

Next, we removed the effects of continental ice volume from the published MD03-2707 $\delta^{18}O_{sw}$ record from Weldeab et al. (2007) using the same deglacial record of sea level change from Waelbroeck et al. (2002) (Fig. 4B). A comparison of the two records shows similar IVF-$\delta^{18}O_{sw}$ values from the LGM until H1. During H1, IVF-$\delta^{18}O_{sw}$ values in the Gulf of Guinea decrease, in contrast to the IVF-$\delta^{18}O_{sw}$ increase in the Niger Delta. At the onset of the BA, calculated IVF-$\delta^{18}O_{sw}$ values in both records become lighter, indicating fresher conditions at both sites, but the magnitude and abruptness of this freshening is far greater in MD03-2707 (Fig. 4B). During the YD, both records once again record more positive IVF-$\delta^{18}O_{sw}$ values, suggesting an increase in regional salinity during this event. The largest offset between the two records occurs during the Holocene, where the Niger Delta values are considerably more positive than those in the Gulf of Guinea, likely due to the location of MD03-2707 in an area of lower modern salinity (Fig. 1).

Although the Fan 17 IVF-$\delta^{18}O_{sw}$ record shares some similarities with the nearby record of MD03-2707, significant variability in the Fan 17 IVF-$\delta^{18}O_{sw}$ record makes it difficult to interpret with confidence. While Charles and Fairbanks (1990) established the linear relationship between $\delta^{18}O_{sw}$ and SSS, this relationship relies on knowledge of the regional $\delta^{18}O_{sw}$ endmembers. As the

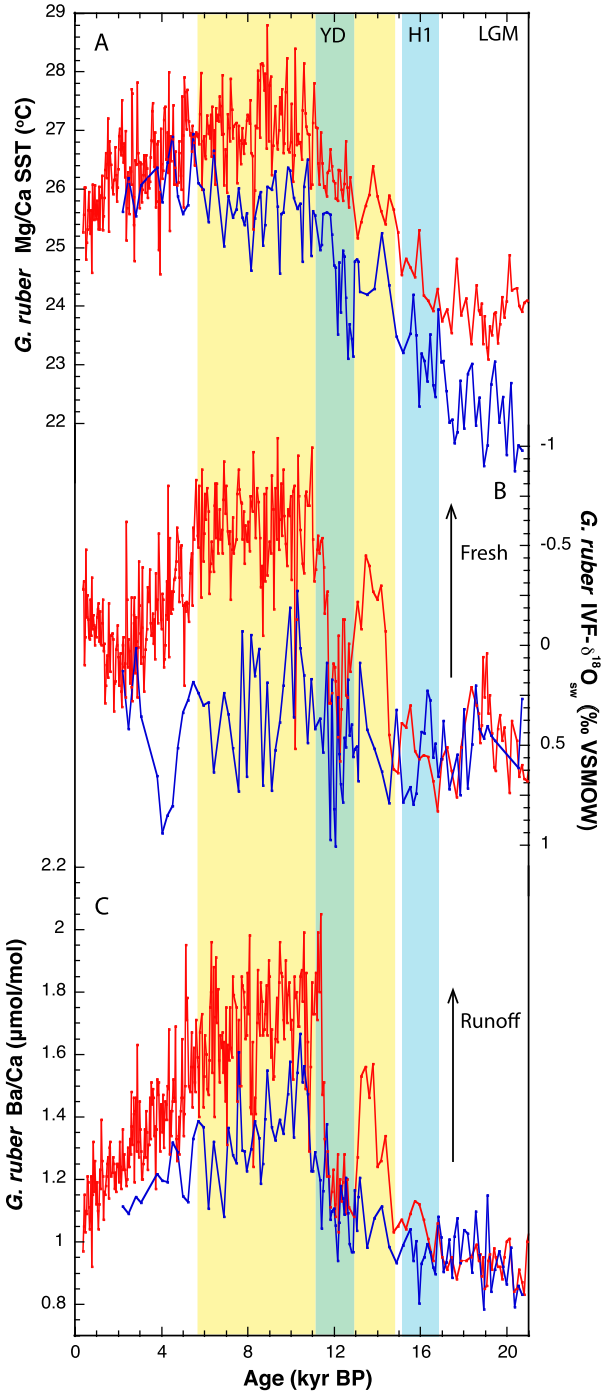

Fig. 4. Comparison of records from Fan 17 (blue) and MD03-2707 (red) in the eastern Gulf of Guinea (Weldeab et al., 2007). (A) *G. ruber* Mg/Ca derived SST (°C). (B) Calculated IVF-$\delta^{18}O_{sw}$. (C) *G. ruber* Ba/Ca (μmol/mol). For both MD03-2707 and Fan 17 $\delta^{18}O_{sw}$ records we calculated ice-volume free $\delta^{18}O_{sw}$ (IVF-$\delta^{18}O_{sw}$) to account for any trend resulting from changes in continental ice volume. Increased deglacial wetness begins at 17 kyr in MD03-2707, and the nature of variability in this core is far more abrupt compared to the Niger Delta. MD03-2707 records are likely influenced mainly by Central African runoff, whereas Fan 17 records are influenced by the WAM. The Holocene offset reflects the fresher conditions at MD03-2707 and the modern SSS gradient between sites. Light blue boxes mark H1 and the YD, and yellow box indicates the AHP. (For interpretation of the references to color in this figure legend, the reader is referred to the web version of this article.)

majority of freshwater reaching the Fan 17 site is sourced almost entirely from the Niger River, changing moisture trajectories in the past would have changed the $\delta^{18}O_{sw}$:SSS relationship. The $\delta^{18}O$ of Niger River runoff is an integration of precipitation that falls across the large river basin with a significant latitudinal range (Fig. 1). Moisture in this area today is sourced mainly from the EEA with moisture from temperate latitudes playing a lesser role (Nicholson, 2013). However, changes in the relative contributions to rainfall from other regions, especially during cold events when northerly winds had more prominence across West Africa (McGee et al., 2010), would have undoubtly changed the $\delta^{18}O$ value of Niger River runoff and thus the regional $\delta^{18}O_{sw}$:SSS relationship. In contrast, the MD03-2707 core is located near equatorial drainage basins and is also in the low salinity core of the Gulf of Guinea, thus reducing these effects. When the WAM was reduced, rainfall would have been concentrated in the southern regions of the Niger River catchment area, resulting in more positive freshwater $\delta^{18}O$ values relative to today. Also, changes in upwelling strength and duration have also been shown to cause significant deviations in local $\delta^{18}O_{sw}$:SSS relationships (McConnell et al., 2009). These complications likely contribute to the variability in our Niger Delta IVF-$\delta^{18}O_{sw}$ record, so we choose to limit interpretation of SSS change based on this record, and instead turn to the Fan 17 *G. ruber* Ba/Ca record.

4.3. Ba/Ca record

In order to reconstruct the discharge history of the Niger River, we measured Ba/Ca ratios in *G. ruber* from Fan 17. The desorption of Ba^{2+} from suspended sediments in riverine water makes the [Ba^{2+}] in river water much higher than in seawater. Dissolved Ba^{2+} in river water exhibits conservative mixing with seawater, resulting in a linear inverse correlation between salinity and [Ba^{2+}] (Coffey et al., 1997). In addition, laboratory experiments have shown that the incorporation of Ba^{2+} into foraminiferal calcite is linearly dependent on the [Ba^{2+}] of the water in which the shell precipitates (Honisch et al., 2011). Thus, Ba/Ca ratios in planktonic foraminifera can be used to estimate past changes of riverine input. Given the close proximity between Fan 17 and the Niger River Delta, and the river's large discharge volume, it is logical to assume that periods of elevated Ba/Ca ratios reflect increased rates of discharge from the Niger River.

The Fan 17 Ba/Ca record indicates the lowest Ba/Ca ratios of ~0.9 μmol/mol during the LGM (Fig. 3E). Ba/Ca ratios remain relatively constant between 20 and 15 kyr (within error), oscillating around $\sim 1.0 \pm 0.1$ μmol/mol. There is not a significant change in Ba/Ca values during the transition from the LGM into H1 in the Niger Delta (Fig. 3E). At 14.8 kyr, Ba/Ca ratios begin to gradually increase from 1.0 to 1.2 μmol/mol throughout the duration of the BA. During the YD, Ba/Ca ratios show a minor decrease to ~1.1 μmol/mol (Fig. 3E). Although previous reconstructions of paleohydrological changes in West Africa found evidence for a dramatic decrease in precipitation at the start of the YD (Collins et al., 2013; Mulitza et al., 2008; Tjallingii et al., 2008), the Ba/Ca record from Fan 17 indicates only a minor reduction of Niger River discharge at the start of the YD. Finally, peak Ba/Ca ratios are recorded during the early Holocene at 10.5 kyr and then gradually decrease over the Holocene.

Weldeab et al. (2007) also generated a Ba/Ca record using *G. ruber* from the nearby Gulf of Guinea core MD03-2707 (Fig. 4C). Despite being located over 400 km southeast of the nearest Niger River distributary, the MD03-2707 record was interpreted to reflect Niger River runoff and WAM variability. A detailed inspection of modern Gulf of Guinea SSS, however, suggests that rivers draining Equatorial Africa such as the Sanaga, Ogooue, and Congo Rivers also contribute significantly to the very low salinities at MD03-2707 due to north-directed surface currents (Fig. 1) (Hopkins et al., 2013; Jobe et al., 2011). This additional freshwater causes the SSS at MD03-2707 to be fresher than at Fan 17 today (Fig. 1). Although the Guinea Current carries a component of the Niger River plume east, it is likely that SSS in the area of MD03-2707 is influenced by a number of equatorial freshwater sources, and thus the signal reflects a combination of Equatorial African and WAM variability.

A comparison of our Ba/Ca record from the Niger Delta with the previously published Ba/Ca record from MD03-2707 (Fig. 4C) shows both records are broadly similar, with an overall correlation coefficient of $r = 0.79$. As was the case with the IVF-$\delta^{18}O_{sw}$ comparison, Ba/Ca values in both records between 17–20 kyr are remarkably similar, indicating that low SSS and reduced river discharge conditions were widespread throughout the entire Gulf of Guinea and Niger Delta prior to H1 (Fig. 4). However, the similarities break down particularly between 17.5 kyr and 13 kyr when the weakest correlation between records exists ($r = 0.6$; Fig. 4C). Prior to the start of H1 around 17.5 kyr, MD03-2707 Ba/Ca ratios gradually increase by +0.2 μmol/mol or ~15% of the LGM-Holocene amplitude, indicating an initial increase in riverine discharge at this location until ~13 kyr. In contrast, Ba/Ca ratios at Fan 17 continue to record dry, LGM-like values through H1 until 14.8 kyr (Fig. 4). Then, beginning at the start of the AHP around 14.8 kyr and lasting until 13 kyr, Fan 17 Ba/Ca ratios steadily begin to record increased riverine discharge (+0.25 μmol/mol) across this interval. This increase is more gradual than the transition in MD03-2707 over the same interval, where the magnitude of Ba/Ca ratio increase is twice that of Fan 17 and occurs in nearly half the time (Fig. 4C). The responses between locations remain different during the YD as well. *G. ruber* Ba/Ca ratios in MD03-2707 abruptly decrease by 0.5 μmol/mol in less than a few centuries starting at 13 kyr, whereas Ba/Ca ratios in Fan 17 decrease only slightly at the start of the YD. Interestingly, both records once again record similar Ba/Ca values during the YD period. Following the end of the YD, the Ba/Ca records in both cores record an abrupt increase in riverine discharge as the African Monsoon systems reached peak intensity at this time. Conditions remain fresher at site MD03-2707 for the duration of the Holocene, reflecting modern hydrographic conditions (Figs. 1, 4C).

We interpret the deglacial differences between the Fan 17 and MD03-2707 Ba/Ca records as the result of riverine discharge from two different rainfall systems. We hypothesize that the Ba/Ca record from MD03-2707 does not solely reflect WAM processes. The influence of equatorial rainfall on MD03-2707 is illustrated by a comparison with the δD_{wax} humidity record from core GeoB-6518 (Weijers et al., 2007) located at the Congo River outflow (Fig. 5B). This record shows that moisture across the Equatorial African tropics, in particular the Congo Basin, began to gradually increase starting at 17 kyr (Schefuß et al., 2005; Weijers et al., 2007) and continued to increase until 13 kyr, when arid conditions abruptly interrupted the moisture increase (Fig. 5B). A companion record of $\delta^{18}O_{sw}$ from the same core (GeoB-6518) also reveals a freshening of waters near the Congo River outlet starting at around 17 kyr (Schefuß et al., 2005). Although drought conditions have been indicated across the Equatorial African tropics during H1, highlighted in particular by the desiccation of East African rift lakes (Gasse et al., 2008; Stager et al., 2011), these lakes lie in the region east of the Rwenzori Mountains that border The Congo and Uganda rivers. The Rwenzori Mountains constrain the location of the Congo Air Boundary where unstable air from the Congo Basin and Indian Ocean converge to produce much of the seasonal rainfall across the African Rift Valley (Tierney et al., 2011). This uniquely different set of precipitation dynamics, combined with significantly different forcing influences including Indian Ocean SST (Tierney et al., 2013), most likely resulted in different rainfall pat-

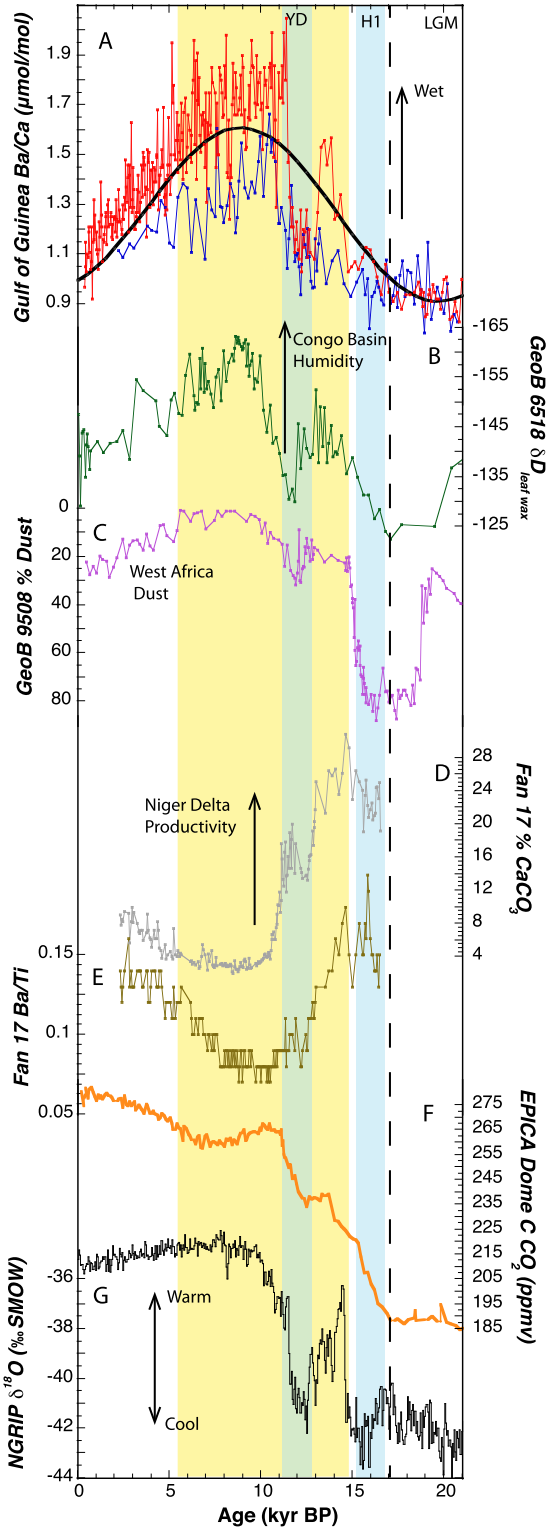

Fig. 5. Evolution of West and Central African hydroclimate during the last deglacial. (A) Ba/Ca records from the Niger Delta (blue) and MD03-2707 (red) with 11°N summer time insolation superimposed (black). (B) δD record of Congo River Basin humidity from GeoB 6518 Weijers et al. (2007). (C) % dust in core GeoB 9508 (15.29°N, 17.56°W) from Collins et al. (2013). (D) Fan 17 % total carbonate and (E) Ba/Ti. (F) EPICA Dome CO_2 Monnin et al. (2004) and (G) NGRIP ice core $\delta^{18}O$. Black dashed line represents the initial intensification of rainfall in MD03-2707 and Congo River Basin at the onset of increasing CO_2 levels. At the onset of abrupt Northern Hemisphere warming around 14.8 kyr, the tropical rainbelt intensifies throughout West and Central Africa, but is slow to reach maximum strength across interior West Africa as the rainbelt gradually tracks northward with increasing insolation. During the H1 and YD events, large increases in dust flux from West Africa occur (C) despite no major change in hydroclimate across this region. Increased wind strength stimulated coastal upwelling enhancing primary productivity during the H1 and YD (D, E). Wind intensification also likely drove the concurrent dust emissions during H1 and the YD. (For interpretation of the references to color in this figure legend, the reader is referred to the web version of this article.)

terns between the East Africa, Equatorial Congo and West African regions during H1 (Fig. 1).

4.4. Regional response to climate forcings

The differences between our new Niger Delta records and the previously published MD03-2707 records reveal new insights into the evolution of precipitation throughout Western and Equatorial Africa during the last deglaciation. Today, annual to decadal variability results from changes in the intensity or latitudinal extent of the rainbelt, which produces two distinct rainfall patterns between West and Equatorial Africa (Nicholson, 2009). A dipole pattern results from changes in the latitudinal excursion of the rainbelt causing West Africa to dry when Equatorial Africa becomes wet, and vice versa. In contrast, both regions vary in phase with one another during changes in rainbelt intensity (Nicholson, 2008; Nicholson and Grist, 2001). Long-term variability of these patterns stems from their sensitivity with respect to varying climatic forcings. While both regions are likely to be influenced to some degree by changes in high latitude Northern Hemisphere climate, a recent modeling study found that greenhouse gas concentrations are especially important for precipitation across Equatorial Africa, whereas West Africa is more sensitive to Northern Hemisphere summer insolation (Otto-Bliesner et al., 2014).

Dry conditions at Fan 17, MD03-2707, and GeoB-6518 during the LGM indicates that the strength of the tropical rainbelt was significantly reduced region-wide, corresponding to low atmospheric [CO_2] and precessional forcing at this time (Fig. 5A and F). An increase in precipitation along coastal regions of Tropical Africa and continued aridity in the WAM region across H1 suggests a possible dipole. Increasingly wet conditions across Equatorial Africa, likely responding to rising CO_2 levels by the start of H1 imply a gradual strengthening of the rainbelt during this time (Collins et al., 2011). Meanwhile, in West Africa, continued low discharge at the Niger Delta suggests that the rainbelt had not yet reached latitudes far enough North to stimulate significant rainfall across the Sahel and in the Niger River drainage basin (Fig. 1). Similar limitations of the northward extent of the global rainbelt during H1 have been documented (Leduc et al., 2009; Peterson et al., 2000). Therefore, our data would suggest the Sahara and Sahel continued to experience dry conditions similar to the LGM for the duration of H1, in spite of increased dust fluxes during this time, suggesting an intensification of drought in West Africa (McGee et al., 2013; Mulitza et al., 2008) (Fig. 5C). Given the absence of any major change in West African precipitation in our new records during H1, our Niger Delta records suggest that increased wind strength, rather than intensified drought, most likely explains the increased dust emissions from the Sahara and Sahel during H1. It is only after H1, possibly in response to Northern Hemisphere warmth during the BA and increased precessional insolation, that our new records indicate the start of an intensification of rainfall across West Africa (Fig. 5A). The delayed response of our Niger Delta records compared to those in MD03-2707 likely reflects the steady northward progression of the rainbelt's seasonal extreme in response to gradually increasing summertime insolation across this interval.

This may help explain the discrepancy between the Fan 17 Ba/Ca record of Niger River discharge change and regional coastal precipitation changes recorded in the δD values of leaf wax in sediment cores from Lake Bosumtwi in Southern Ghana (Shanahan et al., 2015) and near the Senegal River mouth (Niedermeyer et al., 2010). Unlike the Fan 17 Ba/Ca record, the Lake Bosumtwi

and coastal Senegal reconstructions show a significant H1 drying relative to the LGM. However, this is not surprising because the evolution of the monsoon can be summed up into three parts: an "oceanic phase" during winter when the rainbelt is situated just north of the equator, a "coastal phase" when the rainbelt migrates over coastal Africa in early spring where it remains through July until the monsoon jumps to a "Sahelian phase" in mid-July (Thorncroft et al., 2011). This jump is the result of two processes. First, the northward shift is ultimately controlled by the latitudinal temperature gradient setup across West Africa in summer, and secondly, the rainbelt remains at the coast rather than migrating inland due to the persistence of warm water along the Guinea Coast. Thus, the location of Lake Bosumtwi at 6°N means it receives nearly all of its precipitation during the "coastal phase". In addition, the sediment core used by Niedermeyer et al. (2010) records, in part, coastal precipitation changes over the Senegal River drainage basin extending as far south as 10°N. Although these authors argue aeolian processes contribute to leaf wax supply at their study site, they cannot rule out riverine input from the Senegal River. Regardless, their study site would be sensitive to vegetation changes along the coastal margin of Africa. During H1, in response to cooler Northern Hemisphere conditions, the rainbelt was likely locked into the oceanic phase longer, spending less time over the coastal African margin and the Guinea Coast relative to the LGM and causing a decrease in precipitation at Lake Bosumtwi and in the Senegal drainage basin.

To the north across the Niger River Basin, the monsoon jump either failed to occur or had yet to penetrate far enough into interior West Africa that the difference in rainfall between the LGM and H1 was negligible from the Niger River. Furthermore, Ba/Ca ratios in Fan 17 from the LGM through H1 are near modern marine endmember values for this region (Edmond and Boyle, 1978), limiting the foramiferal Ba/Ca proxy to record reductions in Niger River discharge beyond a certain threshold. Therefore, changes in Ba/Ca ratios in Fan 17 may underestimate changes in Niger River discharge during a dry climate state such as the period between the LGM and H1. For this reason, we cannot rule out the possibility that there was indeed a shift to drier conditions over the Niger Delta region during H1, consistent with other coastal precipitation proxies.

4.5. Niger Delta primary productivity

The dominant current influencing our study site at Fan 17 along the western Niger Delta is the eastward flowing Guinea Current. Given the prevalence and strength of the Guinea Current in this region, we feel it is unlikely that a significant change in the dominant current direction occurred in the past. Therefore, sediment transport from the Niger Delta to Fan 17 likely remained constant through time, allowing for us to compare the timing of bulk sediment geochemistry variability with changes recorded in planktonic foraminifera from the site. In contrast, study sites located farther to the east in the Gulf of Guinea, where the Guinea Current meets northward flowing currents along the equatorial margin, are susceptible to changing sediment supply through time. In particular, increased exposure of the Bight of Bonny during periods of sea level low stands likely blocked a portion of eastward flow of the Guinea Current. This may have significantly reduced the amount of suspended sediment from the Niger Delta delivered to the western side of the Bight, including the site used in the Weldeab et al. (2007) study.

At the beginning of the YD, Northern Hemisphere cooling helped to trigger a return to arid conditions and a large-scale weakening of rainbelt intensity in Equatorial Africa. While it appears that West Africa did experience some degree of drying during this time, our Niger Delta records do not suggest that the reduction in moisture was nearly as severe as it was in Equatorial Africa. Nevertheless, significant dust emissions are still associated with the YD (McGee et al., 2013; Mulitza et al., 2008) (Fig. 5C). It is unlikely that the small change in aridity suggested by our Niger Delta Ba/Ca record would result in such a large change in dust flux. Instead, stronger winds during the YD likely caused the elevated dust emissions, but the magnitude of flux may have been limited by increased vegetation coverage at this time (deMenocal et al., 2000).

Our elemental Ba/Ti and total carbonate data provide additional support to the role of wind-driven dust emissions during H1 and the YD. Elevated Ba/Ti ratios in Fan 17 suggest increased surface productivity, as the excess rain of organic matter settling through the water column promotes the additional formation of barite in sediments relative to the terrigenous flux (inferred from Ti) (Murray and Leinen, 1996; Murray et al., 2000). Total carbonate content also tracks the increased rain of calcareous organisms to the seafloor during production blooms. Ba/Ti ratios and total carbonate values are highest during H1 (Fig. 5D and E) before decreasing during the BA. A second, albeit smaller increase occurs during the YD, followed by a second decrease to the lowest values during the early Holocene before gradually increasing at 7 kyr.

Although primary productivity around the Niger Delta is nearly constant throughout the year, productivity levels are generally low due to macronutrient limitations of phosphate and nitrate. Declining productivity at a time of increasing Niger River discharge starting at ~15 kyr in Fan 17 suggests that Niger River discharge was not an important source of nutrients to the region at this time. Furthermore, significant dilution of the Ba/Ti and $\%CaCO_3$ record from Fan 17 at this time is also unlikely, given the large magnitude of decrease in these measurements beginning at ~15 kyr with respect to the minimal increase in river discharge implied by the *G. ruber* Ba/Ca record across the BA. However, productivity does appear to correlate well with regional dust flux (Figs. 5C, D, E). Although dust alone could not provide the macronutrients necessary to stimulate excess productivity, the strong winds associated with increased dust emissions during H1 and the YD would have blown over the Niger Delta and enhanced coastal upwelling. Stronger upwelling would supply surface waters offshore of the Niger Delta with increased levels of phosphate and nitrate to fuel greater productivity. In addition, *G. ruber* $\delta^{13}C$ values from Fan 17 are most depleted during H1 and the YD, lending support to our conclusion of enhanced wind-driven upwelling in the Niger Delta during these cold intervals (see Supplemental Fig. 1). Although increased upwelling of isotopically light subsurface waters in response to stronger upwelling probably cannot explain all of the decrease in *G. ruber* $\delta^{13}C$ values during H1 and the YD (Schmittner and Lund, 2015), this trend is consistent with our conclusion that wind driven upwelling increased during both H1 and the YD. Interestingly, minimum productivity over the last 17 kyr occurs during the peak of the AHP (7–11 kyr) when conditions were the wettest, emphasizing the importance of wind-driven upwelling over river discharge in driving productivity in the Niger Delta. The gradual decline of productivity between 12.9–15 kyr relative to the abrupt decrease in dust at ~15 kyr can be likened to observations of modern dust plumes, where a cubic relationship between wind strength and dust emission demonstrates how the top wind strengths account for the majority of dust activation. Therefore, a minor change in wind strength can result in a large decrease in dust emission (McGee et al., 2010).

This wind driven upwelling off the Niger Delta is likely driven by the intensification of the boreal winter Harmattan wind over the area during H1 and the YD. Under modern climate conditions during boreal winter, the northeasterly Harmattan wind progressively replaces the southwesterly monsoon flow across the Sahel and Guinea coast as the rainbelt reaches its most southerly posi-

tion (Lyngsie et al., 2011). The Harmattan largely contributes to the wintertime dust plume, sourcing dust mainly from the Bodele Depression, the single largest dust source in West Africa (Washington et al., 2009). Although the Bodele Depression remains active year round, maximum dust emissions occur during winter months in association with the Harmattan wind (Washington et al., 2009). One possibility is that throughout H1, the intensified Harmattan winds during the dry season would have lofted significantly more dust into the atmosphere while also producing longer and more vigorous upwelling, sustaining increased productivity in the Niger Delta. A similar scenario may have also characterized the YD, but vegetation reconstructions suggest that much of the Bodele Depression was largely vegetated by this time, and would not have produced similar volumes of dust (Cockerton et al., 2014).

Nevertheless, as we discussed above, it is likely that areas along the coast of Africa did indeed become drier during H1 relative to the LGM. Niedermeyer et al. (2010) argued that increases in δD leaf wax values at their study site on the Senegal coast suggest a drier wet season along the African coastal zone during H1 and the YD. Although it is likely that drier wet season conditions over coastal Africa also contributed to increased dust fluxes at other study sites along the West African Margin during cold stadials (McGee et al., 2013), it is unlikely that the heavily vegetated coastal regions contributed a significant amount of additional dust, even if summers were drier. In addition, leaf wax δ^{13}C values from the Senegal coast do not suggest a significant shift from C_3 to C_4 plants during either H1 or the YD, providing evidence that the drier conditions at these times may have had little effect on the coastal vegetation (Niedermeyer et al., 2010).

Following the YD, peak wetness and a northerly position of the rainbelt limited the influence of the Harmattan, resulting in low dust fluxes across West Africa and decreased productivity at the Niger Delta. Upon the return of Northern Hemisphere warmth at ~11.5 kyr, peak rainbelt intensity was quickly reached in response to maximum insolation and greenhouse gas forcing, and persisted for several thousand years during the early Holocene. An abrupt decrease in Niger River discharge at ~5.7 kyr shown by Fan 17 (Fig. 5A) is consistent with the timing and abruptness of the AHP termination in other records from West Africa (deMenocal et al., 2000; Shanahan et al., 2015), whereas father to the south in MD03-2707 the end of the AHP occurs slightly later at 4.9 kyr. Furthermore, the gradual decrease in the SSS gradient between the Niger Delta and MD03-2707 during the Holocene may reflect a long-term decrease in the intensity of the rainbelt associated with decreasing insolation over this interval (Fig. 5A).

5. Conclusions

Taken together with previous reconstructions of West African precipitation changes, our new deglacial records of SSS change in the Niger Delta and Niger River discharge variability suggest temporal and spatial offsets in the timing of the WAM and Equatorial monsoon systems in Central Africa. While atmospheric advection of moisture into the interior of Equatorial Africa seems to have begun at or near the start of H1, moisture delivery to the Sahel region did not initiate until after the start of the AHP at around 14.8 kyr. In addition, our findings help explain the large increase of dust emissions during H1 and the YD, suggesting that these changes were driven by both elevated winds and a drier African coastal zone. Therefore, this study places existing dust reconstructions in the context of changing wind and aridity conditions across West Africa and provides a new framework for interpreting dust records in West Africa. This framework decreases uncertainty in interpreting dust records that has limited climate modeling abilities to simulate the role of dust in past climate change, which often underestimates critical parameters required for forecasting the regional response of African dust to future climate change (Evan et al., 2014). Moreover, our results lend support to the correlation between the WAM strength and summer insolation variability over longer time scales. In the future, precessional insolation will remain at near minimum values in the Northern Hemisphere tropics and thus prolonged droughts plaguing this region will likely persist or intensify. Despite this, further understanding of the causes for drought across West Africa will lead to better drought prediction and readiness for developing nations and improve the quality of life for those living in the region.

Acknowledgements

We thank L. Romero for assistance with geochemical analyses and lab instruments. We also thank S.E. Nicholson for useful discussions on West African meteorology. This work was funded by a National Science Foundation grant to M.W.S. (OCE-1102743) and Shell International Exploration and Production, Inc.

Appendix A. Supplementary material

Supplementary material related to this article can be found online at http://dx.doi.org/10.1016/j.epsl.2016.05.038.

References

Anand, P., Elderfield, H., Conte, M.H., 2003. Calibration of Mg/Ca thermometry in planktonic foraminifera from a sediment trap time series. Paleoceanography 18 (2).
Bemis, B.E., Spero, H.J., Bijima, J., Lea, D.W., 1998. Reevaluation of the oxygen isotopic composition of planktonic foraminifera: experimental results and revised paleotemperature equations. Paleoceanography 13 (2), 150–160.
Chang, P., Zhang, R., Hazeleger, W., Wen, C., Wan, X.Q., Ji, L., Haarsma, R.J., Breugem, W.P., Seidel, H., 2008. Oceanic link between abrupt changes in the North Atlantic Ocean and the African monsoon. Nat. Geosci. 1 (7), 444–448.
Charles, C.D., Fairbanks, R.G., 1990. Glacial to interglacial changes in the isotopic gradients of southern ocean surface water. In: Bleil, U., Thiede, J. (Eds.), Geological History of the Polar Oceans: Arctic Versus Antarctic. Kluwer, Netherlands, pp. 519–538.
Cockerton, H.E., Holmes, J.A., Street-Perrott, F.A., Ficken, K.J., 2014. Holocene dust records from the West African Sahel and their implications for changes in climate and land surface conditions. J. Geophys. Res., Atmos. 119 (14), 8684–8694.
Coffey, M., Dehairs, F., Collette, O., Luther, G., Church, T., Jickells, T., 1997. The behaviour of dissolved barium in estuaries. Estuar. Coast. Shelf Sci. 45 (1), 113–121.
Collins, J.A., Govin, A., Mulitza, S., Heslop, D., Zabel, M., Hartmann, J., Rohl, U., Wefer, G., 2013. Abrupt shifts of the Sahara–Sahel boundary during Heinrich stadials. Clim. Past 9 (3), 1181–1191.
Collins, J.A., et al., 2011. Interhemispheric symmetry of the tropical African rainbelt over the past 23,000 years. Nat. Geosci. 4 (1), 42–45.
deMenocal, P., Ortiz, J., Guilderson, T., Adkins, J., Sarnthein, M., Baker, L., Yarusinsky, M., 2000. Abrupt onset and termination of the African Humid Period: rapid climate responses to gradual insolation forcing. Quat. Sci. Rev. 19 (1–5), 347–361.
Edmond, J.M., Boyle, E., 1978. Desorption of barium in the plume of the Zaire (Congo) river. Neth. J. Sea Res. 12 (3–4), 324–328.
Evan, A.T., Flamant, C., Fiedler, S., Doherty, O., 2014. An analysis of aeolian dust in climate models. Geophys. Res. Lett. 41 (16), 5996–6001.
Gasse, F., Chalie, F., Vincens, A., Williams, M.A.J., Williamson, D., 2008. Climatic patterns in equatorial and southern Africa from 30,000 to 10,000 years ago reconstructed from terrestrial and near-shore proxy data. Quat. Sci. Rev. 27 (25–26), 2316–2340.
Hertzberg, J.E., Schmidt, M.W., 2013. Refining Globigerinoides ruber Mg/Ca paleothermometry in the Atlantic Ocean. Earth Planet. Sci. Lett. 383, 123–133.
Honisch, B., Allen, K.A., Russell, A.D., Eggins, S.M., Bijma, J., Spero, H.J., Lea, D.W., Yu, J., 2011. Planktic foraminifers as recorders of seawater Ba/Ca. Mar. Micropaleontol. 79, 52–57. http://dx.doi.org/10.1016/j.mar.micro.2011.01.003.
Hopkins, J., Lucas, M., Dufau, C., Sutton, M., Stum, J., Lauret, O., Channelliere, C., 2013. Detection and variability of the Congo River plume from satellite derived sea surface temperature, salinity, ocean colour and sea level. Earth Planet. Sci. Lett. 139, 365–385.
Itiveh, K.O., Bigg, G.R., 2008. The variation of discharge entering the Niger Delta system, 1951–2000, and estimates of change under global warming. Int. J. Climatol. 28 (5), 659–666.
Jobe, Z.R., Lowe, D.R., Uchytil, S.J., 2011. Two fundamentally different types of submarine canyons along the continental margin of Equatorial Guinea. Mar. Pet. Geol. 28, 843–860.

Leduc, G., Vidal, L., Tachikawa, K., Bard, E., 2009. ITCZ rather than ENSO signature for abrupt climate changes across the tropical Pacific? Quat. Res. 72 (1), 123–131.
Lyle, M., Olivarez Lyle, A., Gorgas, T., Holbourn, A., Westerhold, T., Hathorne, E., Kimoto, K., Yamamoto, G., 2012. Data report: raw and normalized elemental data along the site U1338 splice from X-ray fluorescence scanning. In: Proceedings of the International Ocean Drilling Program. 320/321.
Lyngsie, G., Awadzi, T., Breuning-Madsen, H., 2011. Origin of Harmattan dust settled in Northern Ghana – long transported or local dust? Geoderma 167–168, 351–359.
McConnell, M.C., Thunell, R.C., Lorenzoni, L., Astor, Y., Wright, J.D., Fairbanks, R., 2009. Seasonal variability in the salinity and oxygen isotopic composition of seawater from the Cariaco Basin, Venezuela: implications for paleosalinity reconstructions. Geochem. Geophys. Geosyst. 10.
McGee, D., Broecker, W.S., Winckler, G., 2010. Gustiness: the driver of glacial dustiness? Quat. Sci. Rev. 29 (17–18), 2340–2350.
McGee, D., deMenocal, P.B., Winckler, G., Stuut, J.B.W., Bradtmiller, L.I., 2013. The magnitude, timing and abruptness of changes in North African dust deposition over the last 20,000 yr. Earth Planet. Sci. Lett. 371, 163–176.
McManus, J.F., Francois, R., Gherardi, J.-M., Keigwin, L.D., Brown-Leger, S., 2004. Collapse and rapid resumption of Atlantic meridional circulation linked to deglacial climate changes. Nature 428 (22), 834–837.
Monnin, E., Steig, E.J., Siegenthaler, U., Kawamura, K., Schwander, J., Stauffer, B., Stocker, T.F., Morse, D.L., Barnola, J.-M., Bellier, B., Raynaud, D., Fischer, H., 2004. Evidence for substantial accumulation rate variability in Antarctica during the Holocene, through synchronization of CO_2 in the Taylor Dome, Dome C and DML ice cores. Earth Planet. Sci. Lett. 224, 45–54. http://dx.doi.org/10.1016/j.epsl.2004.05.007.
Mulitza, S., Prange, M., Stuut, J.B., Zabel, M., von Dobeneck, T., Itambi, A.C., Nizou, J., Schulz, M., Wefer, G., 2008. Sahel megadroughts triggered by glacial slowdowns of Atlantic meridional overturning. Paleoceanography 23 (4).
Murphy, L.N., Clement, A.C., Albani, S., Mahowald, N.M., Swart, P., Arienzo, M.M., 2014. Simulated changes in atmospheric dust in response to a Heinrich stadial. Paleoceanography 29 (1), 30–43.
Murray, R.W., Leinen, M., 1996. Scavenged excess aluminum and its relationship to bulk titanium in biogenic sediment from the central equatorial Pacific Ocean. Geochim. Cosmochim. Acta 60 (20), 3869–3878.
Murray, R.W., Knowlton, C., Leinen, M., Mix, A.C., Polsky, C.H., 2000. Export production and terrigenous matter in the Central Equatorial Pacific Ocean during interglacial oxygen isotope Stage 11. Glob. Planet. Change 24, 59–78.
Nicholson, S.E., 2008. The intensity, location and structure of the tropical rainbelt over west Africa as factors in interannual variability. Int. J. Climatol. 28 (13), 1775–1785.
Nicholson, S.E., 2009. A revised picture of the structure of the "monsoon" and land ITCZ over West Africa. Clim. Dyn. 32 (7–8), 1155–1171.
Nicholson, S.E., 2013. The West African Sahel: a review of recent studies on the rainfall regime and its interannual variability. ISRN Meteorology 2013, 1–32.
Nicholson, S.E., Grist, J.P., 2001. A conceptual model for understanding rainfall variability in the West African Sahel on interannual and interdecadal timescales. Int. J. Climatol. 21 (14), 1733–1757.
Niedermeyer, E.M., Schefuß, E., Sessions, A.L., Mulitza, S., Mollenhauser, G., Schulz, M., Wefer, G., 2010. Orbital- and millennial-scale changes in the hydrologic cycle and vegetation in the western African Sahel: insights from individual plant wax δD and δ^{13}C. Quat. Sci. Rev. 29 (23–24), 2996–3005.
Otto-Bliesner, B.L., Russell, J.M., Clark, P.U., Liu, Z.Y., Overpeck, J.T., Konecky, B., deMenocal, P., Nicholson, S.E., He, F., Lu, Z.Y., 2014. Coherent changes of southeastern equatorial and northern African rainfall during the last deglaciation. Science 346 (6214), 1223–1227.
Peterson, L.C., Haug, G.H., Hughen, K.A., Rohl, U., 2000. Rapid changes in the hydrologic cycle of the Tropical Atlantic during the last Glacial. Science 290, 1947–1951.
Ridley, D.A., Heald, C.L., Prospero, J.M., 2014. What controls the recent changes in African mineral dust aerosol across the Atlantic? Atmos. Chem. Phys. 14, 5735–5747.
Rodriguez, S., Cuevas, E., Prospero, J.M., Alastuey, A., Querol, X., Lopez-Solano, L., Garcia, M.I., Alonso-Perez, S., 2015. Modulation of Saharan dust export by the North African dipole. Atmos. Chem. Phys. 15, 7471–7486.
Schefuß, E., Schouten, S., Schneider, R.R., 2005. Climatic controls on central African hydrology during the past 20,000 years. Nature 437 (7061), 1003–1006.
Schmidt, M.W., Spero, H.J., 2011. Meridional shifts in the marine ITCZ and the tropical hydrologic cycle over the last three glacial cycles. Paleoceanography 26.
Schmidt, M.W., Lynch-Stieglitz, J., 2011. Florida Straits deglacial temperature and salinity change: implications for tropical hydrologic cycle variability during the Younger Dryas. Paleoceanography 26.
Schmidt, M.W., Weinlein, W.A., Marcantonio, F., Lynch-Stieglitz, J., 2012a. Solar forcing of Florida Straits surface salinity during the early Holocene. Paleoceanography 27.
Schmidt, M.W., Chang, P., Hertzberg, J.E., Them, T.R., Link, J., Otto-Bliesner, B.L., 2012b. Impact of abrupt deglacial climate change on tropical Atlantic subsurface temperatures. Proc. Natl. Acad. Sci. USA 109 (36), 14348–14352.
Schmittner, A., Lund, D.C., 2015. Early deglacial Atlantic overturning decline and its role in atmospheric CO_2 rise inferred from carbon isotopes (δ^{13}C). Clim. Past 1, 135–152.
Shanahan, T.M., McKay, N.P., Hughen, K.A., Overpeck, J.T., Otto-Bliesner, B., Heil, C.D., King, J., Scholz, C.A., Peck, J., 2015. The time-transgressive termination of the African Humid Period. Nat. Geosci.
Stager, J.C., Ryves, D.B., Chase, B.M., Pausata, F.S.R., 2011. Catastrophic drought in the Afro-Asian Monsoon region during Heinrich event 1. Science 331 (6022), 1299–1302.
Steph, S., Regenberg, M., Tiedemann, R., Mulitza, S., Nurnberg, D., 2009. Stable isotopes of planktonic foraminifera from tropical Atlantic/Caribbean core-tops: implications for reconstructing upper ocean stratification. Mar. Micropaleontol. 71 (1–2), 1–19.
Stuiver, M., Reimer, P.J., Reimer, R.W., 2013. CALIB Radiocarbon Calibration Version 7.1.
Taylor, S.R., Mclennan, S.M., 1995. The geochemical evolution of the continental-crust. Rev. Geophys. 33 (2), 241–265.
Thorncroft, C.D., Hanh, N., Zhang, C.D., Peyrille, P., 2011. Annual cycle of the West African monsoon: regional circulations and associated water vapour transport. Q. J. R. Meteorol. Soc. 137 (654), 129–147.
Tierney, J.E., Smerdon, J.E., Anchukaitis, K.J., Seager, R., 2013. Multidecadal variability in East African hydroclimate controlled by the Indian Ocean. Nature 493 (7432), 389–392.
Tierney, J.E., Lewis, S.C., Cook, B.I., LeGrande, A.N., Schmidt, G.A., 2011. Model, proxy and isotopic perspectives on the East African Humid Period. Earth Planet. Sci. Lett. 307 (1–2), 103–112.
Tjallingii, R., Claussen, M., Stuut, J.B.W., Fohlmeister, J., Jahn, A., Bickert, T., Lamy, F., Rohl, U., 2008. Coherent high- and low-latitude control of the northwest African hydrological balance. Nat. Geosci. 1 (10), 670–675.
Waelbroeck, C., Labeyrie, L.D., Michel, E., Duplessy, J.C., McManus, J.F., Lambeck, K., Balbon, E., Labracherie, M., 2002. Sea-level and deep water temperature changes derived from benthic foraminifera isotopic records. Quat. Sci. Rev. 21, 295–305.
Wan, X.Q., Chang, P., Saravanan, R., Zhang, R., Schmidt, M.W., 2009. On the interpretation of Caribbean paleo-temperature reconstructions during the Younger Dryas. Geophys. Res. Lett. 36.
Washington, R., Bouet, C., Cautenet, G., Mackenzie, E., Ashpole, I., Engelstaedter, S., Lizcano, G., Henderson, G.M., Schepanski, K., Tegen, I., 2009. Dust as a tipping element: the Bodele depression, Chad. Proc. Natl. Acad. Sci. USA 106 (49), 20564–20571.
Weijers, J.W.H., Schefuss, E., Schouten, S., Damste, J.S.S., 2007. Coupled thermal and hydrological evolution of tropical Africa over the last deglaciation. Science 315 (5819), 1701–1704.
Weldeab, S., Lea, D.W., Schneider, R.R., Andersen, N., 2007. 155,000 years of West African monsoon and ocean thermal evolution. Science 316 (5829), 1303–1307.